Excellent high temperature mechanical properties of Fe2Ni2CrAlx (x= 0.9 to 1.3) multi-principal elements alloys

Ling Qiao [a], Junya Inoue [a b], R.V. Ramanujan [c], Kenji Sekido [a b], Jingchuan Zhu [d]

[a] Institute of Industrial Science, The University of Tokyo, Japan

[b] Department of Materials Engineering, The University of Tokyo, Japan

[c] School of Material Science and Engineering, Nanyang Technological University, Singapore

[d] School of Material Science and Engineering, Harbin Institute of Technology, China

Abstract

The high temperature mechanical properties of a family of Fe2Ni2CrAlx (x=0.9, 1.1, 1.2, 1.3 in molar ratio) multi-principal element alloys (MPEAs) were determined. The initial microstructure and grain size of Fe2Ni2CrAlx MPEAs were characterized. Effect of Al on the density, melting point and mechanical properties at elevated temperature were investigated. Fe2Ni2CrAl1.3 MPEA exhibit the lowest density of 6.78 g/cm3 and highest melting point of (1337.7 ~ 1392.6 °C). The as-cast Fe2Ni2CrAl1.3 MPEA showed an excellent combination of strength and plasticity at elevated temperatures. Fe2Ni2CrAl1.3 MPEA showed high strength of 2119 MPa and 1722 MPa at 200 °C and 400 °C, respectively. The Fe2Ni2CrAlx alloys exhibited exceptional high-temperature plasticity, no fracture occurred even at a compressive strain above 70%. Recrystallization softening appeared at above 600 °C, the transformation of coarse equiaxed grains into subgrains were captured during plastic deformation. Significantly, the specific yield strength of the Fe2Ni2CrAl1.3 MPEA was comparable with traditional Ti based alloys and Ni-based superalloy. The fracture mechanism of Fe2Ni2CrAlx MPEAs was a combination of cleavage and slip separation. Deformation behavior and work hardening ability at elevated temperature were discussed. Finally, finite element method (FEM) was performed to capture the evolution of stress and strain under high-temperature compression.

Keywords

Multi-principal element alloys

Density

Melting point

Mechanical properties

1. Introduction

The conventional strategy of alloy design, involving the addition of a small amount of alloying elements into one primary metal, has been a fundamental practice for many years [1]. Recently, a significant breakthrough in alloying strategy occurred with the discovery of high-entropy alloys (HEAs), also known as multi-principal element alloy (MPEAs) [2], [3]. Unlike conventional alloys, HEAs involve mixing multiple principal elements in roughly equal proportions to achieve a unique microstructure and associated strengthening mechanisms [4]. HEAs have become a highly exciting research topic in the field of materials science, yielding HEAs with unprecedented properties, including high hardness and strength [5], [6], [7], [8], [9], [10], good ductility and toughness [11], [12], [13]. Particularly, HEAs exhibit remarkable mechanical properties at high temperatures [14], [15], [16], [17], [18], [19], [20], their ability to maintain high strength and structural stability under high-temperature conditions makes them appealing for aerospace, power generation, and other high-temperature applications.

In recent years, there has been a significant surge in the design and investigation of MPEAs, including AlCoCrFe [21], [22], [23], [24], AlCoCrFeNi [25], [26], [27], [28], AlCoCrFeNiTi [29], [30], etc. One such group of MPEA systems that has gained substantial attention, especially considering cost-effectiveness, is the quaternary Fe–Ni–Cr–Al based alloy system. This alloy system is of particular interest due to its Co-free nature and potential for achieving high performance. To achieve a favorable balance of high strength and good ductility, recent studies have led to a focus on dual-phase or multi-phase HEAs within these alloy systems. By designing alloys with specific microstructures and phases, researchers aim to harness the synergistic effects of different phases to enhance the overall mechanical properties.

Indeed, elemental composition plays a crucial role in alloy design, particularly in the case of MPEAs. Al is a frequently incorporated element in high-entropy alloys due to its specific characteristics. Al has a relatively large atomic radius, which can influence the lattice structure and phase stability of the resulting alloy. The addition of Al can lead to changes in the crystal structure and affect the formation of solid solutions or intermetallic phases. Incorporating Al into MPEAs can result in solid solution strengthening, enhancing the strength and hardness of MPEAs. Several studies have paid attention to the impact of Al on the microstructure and properties of MPEAs [31], [32], [33], [34], [35], [36]. For example, Wang et al. [33] demonstrated that the addition of Al had a significant impact on the phases, microstructure and mechanical properties of AlxCoCrFeNi HEAs at elevated temperatures, as well as the mechanism for high softening resistance. Kim et al. [35] found that the addition of Al resulted in solute drag creep appearing as the rate-controlling deformation mechanism, the hot workability was greatly improved due to the formation of a BCC phase resulting from addition of Al. Li et al. [37] performed an investigation of the microstructure and properties of AlxCoCrFeMnNi HEAs. With the increasing Al content, the phase changed from single FCC, duplex FCC + BCC to single BCC phase resulting from addition of Al., accompanied by increased microhardness and reduced corrosion resistance. Thus, addition of Al in MPEAs has been demonstrated to exert a substantial influence on alloy properties.

Finite element method (FEM) stands as a pivotal numerical technique essential for elucidating the deformation processes. This method involves discretizing a complex alloy structure into elements, allowing an analysis of the mechanical behavior under various processing conditions. Many studies [38], [39], [40], [41], [42], [43] have demonstrated its practicality in studying the deformation behavior of alloys. Rahul et al. [38] utilized FEM to study the strain distribution and material flow of AlCoCrFeNi2.1 MPEAs during hot deformation, which assisted in predicting actual material flow in the forging process. Li et al. [41] used FEM to quantitatively reveal the underlying correlation between solidification parameters and the morphology. Ahn et al. [42] analyzed the temperature and strain distributions during high-strain-rate compression of CoCrFeMnNi MPEAs, reflecting the local temperature rise in the FEM analysis. FEM enables researchers to simulate how alloys respond to external forces, temperature changes, and other factors, which can predict stress and strain distributions within the alloy during deformation processes such as forging, rolling, extrusion, or other forming operations.

Our previous work [39] has reported a new family of Fe2Ni2CrAlx MPEAs. The crystal structure and microstructural evolution are highly dependent on the Al content, changing from FCC + BCC to BCC + B2 phases. Higher Al content dramatically increased the nanohardness and strength of the Fe2Ni2CrAlx MPEAs. However, the mechanical properties at high temperatures has not been reported.

To boost the potential of Fe2Ni2CrAlx MPEAs in high-temperature application, this work put emphasis on the mechanical properties of Fe2Ni2CrAlx (x = 0.9, 1.1, 1.2, 1.3, where x is the molar ratio of aluminum) at elevated temperatures. The density and melting point were determined to understand the potential for high temperature applications. In addition to experimental work, FEM was performed on Fe2Ni2CrAlx MPEAs to provide insights into factors such as stress distribution, strain patterns, and material flow during the deformation process at elevated temperatures. These findings are expected to further the application of Fe2Ni2CrAlx MPEAs at elevated temperatures.

2. Methodology

2.1. Experimental procedure

The multi-component ingots, with a nominal composition of Fe2Ni2CrAlx (x = 0.9, 1.1, 1.2, 1.3), was prepared through the vacuum arc melting technique. The elemental metals, with boasted a purity exceeding 99.9%, were melted within a water-cooled copper mold. Arc melting were conducted under an atmosphere of ultrahigh-purity argon (Ar). The ingots experienced at least 5 re-melting cycles. The microstructures of the alloys were analyzed using electron backscatter diffraction (EBSD) measurements, which were carried out using a SEM equipped with a EDAX detector and TSL OIM data collection software.

Density of the Fe2Ni2CrAlx MPEAs were measured by using the Archimedes method. Each sample underwent five measurements to obtain averaged values. The solidus and liquidus temperatures were determined using differential scanning calorimetry (DSC). The DSC scans encompassed a temperature range from 25 °C to 1500 °C, at a rate of 10 °C/min during the heating cycles. It maintains a continuous flow of argon (Ar) during the process.

The mechanical properties of the samples were evaluated using compressive tests at elevated temperatures. The compression tests of Φ4mm×6mm cylindrical samples were performed on the AG-X Plus 250 kN/50 kN Electronic Universal Testing Machine. The initial strain rate was 2 mm/min and the temperature was 200 °C, 400 °C, 600 °C and 800 °C. The testing was performed until the fracture of the samples or reaching a reduction of 70%, whichever was earlier. Three compression tests were conducted to derive the average value.

2.2. Finite element simulation

In this work, DEFORM FEM software was utilized for simulating the deformation process of Fe2Ni2CrAlx MPEAs under elevated temperature. The 3D cylindrical sample model was constructed and meshed using the DEFORM-3D Pre tool. Mechanical properties were derived from the stress–strain curves obtained from high-temperature compressive tests, and this data was integrated into the Simufact materials database. Other properties, such as thermal properties, were calculated using the rule of mixtures criterion. The shear friction condition in the FEM simulation was set with an interface friction factor of 0.5 between the die and workpiece interface. The material behavior, temperature distribution, stress levels, and other aspects were obtained to understand the deformation behavior of Fe2Ni2CrAlx MPEAs.

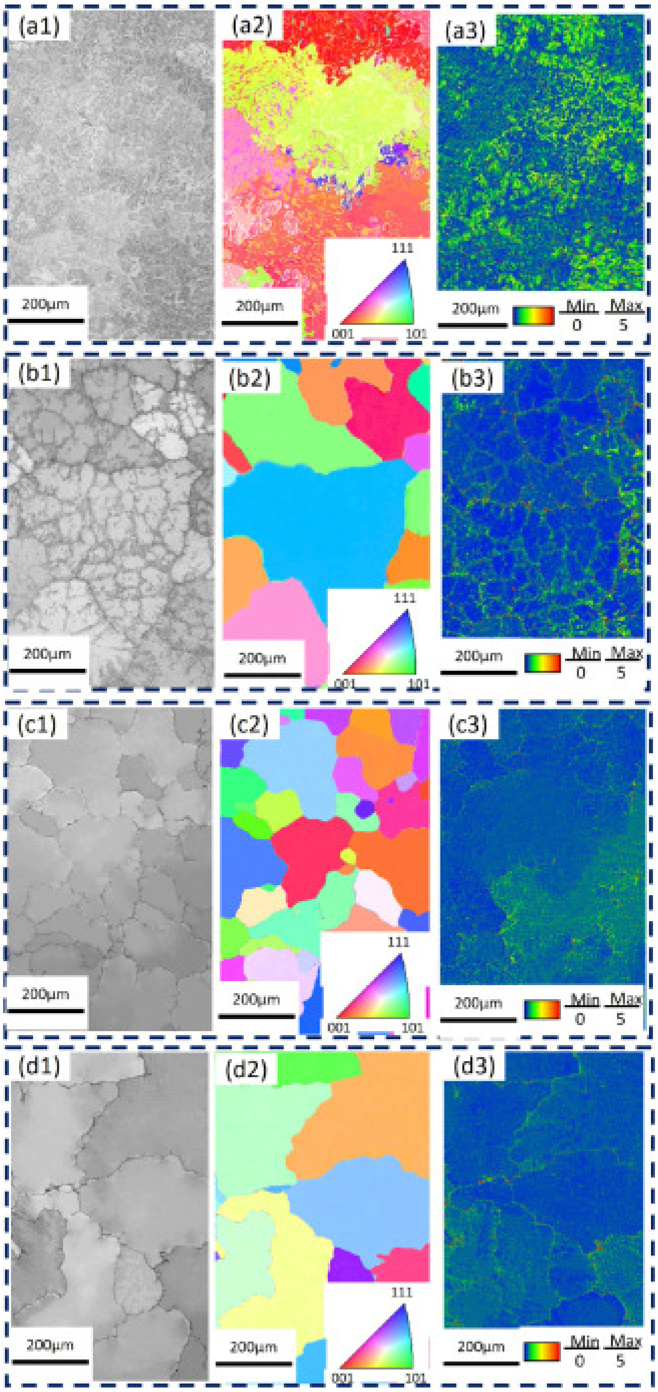

1. Download: Download high-res image (2MB)
2. Download: Download full-size image

Fig. 1. EBSD results of Fe2Ni2CrAlx MPEAs (a1)–(a3) Al0.9, (b1)–(b3) Al1.1, (c1)–(c3) Al1.2, and (d1)–(d3) Al1.3. (For interpretation of the references to color in this figure legend, the reader is referred to the web version of this article.)

3. Results and discussion

3.1. Microstructure

Our preliminary work [39] has reported that Fe2Ni2CrAlx MPEAs (x = 0.9 and 1.1) were composed of the FCC/BCC + B2 phase, which it changed to the BCC + B2 phase structure when the Al content increased to 1.2 and 1.3. The grain boundaries correspond to the Fe–Cr rich BCC phases, the ultrafine phases within the grains were mainly composed of Ni–Al rich B2 phases. To further capture the initial microstructure, Fig. 1 presented the EBSD results of Fe2Ni2CrAlx MPEAs. Fig. 1 (a1)–(d1) and (a2)–(d2) showed the image quality (IQ) maps and inverse pole figure (IPF) maps, respectively. The Fe2Ni2CrAl0.9 MPEA consisted of a high density of small irregularly shaped phases. As the atomic ratio of Al increased to above 1.1, the grain boundary can be clearly observed from IQ images. From EBSD analysis, the grain size values were estimated. The grain size of Fe2Ni2CrAl0.9 MPEA is the largest among these alloys. The Fe2Ni2CrAl1.1 MPEA and Fe2Ni2CrAl1.3 MPEA had similar grain sizes, ~261±93μm and ~280±94μm, respectively. The average grain size of Fe2Ni2CrAl1.2 MPEA was smaller, ~133±96μm. It can be deduced that there is no linear relationship between grain size and Al content. The kernel average misorientation (KAM) maps illustrated the average orientation discrepancies among grains, in which the shift in color from blue to red signifies the variation in orientation from 0° to 5°. Fig. 1 (a3)–(d3) showed that the area within the grain is dominated by blue, showing a low value of KAM. The grain boundary was colored by green, exhibiting a higher value of KAM.

3.2. Density and melting point

The density of Fe2Ni2CrAlx (x = 0.9, 1.1, 1.2, 1.3) MPEAs were summarized in Fig. 2. Among the elements in the studied alloy system (Fe, Ni, Cr, Al), Al has the lowest density, measuring 2.7 g/cm3. It shows the significant influence of Al concentration on the density of alloy. With the atomic ratio of Al element of 0.9, the density of the Fe2Ni2CrAl0.9 alloy is 7.06 g/cm3. When the atomic ratio of Al exceeds 1.1 in the alloy, a reduction in density occurs, bringing it below 7 g/cm3. As the atomic ratio of Al increases from 1.1 to 1.3, the density of the alloy decreases from 6.96 g/cm3 to 6.78 g/cm3. Notably, the prepared Fe2Ni2CrAl1.3 alloy shows the lowest density among the developed compositions. The alloys prepared in this study exhibit significantly lower density than Ni-based superalloys, measuring below 8g/cm3. This characteristic offers a significant advantage for the alloys developed in this research, particularly in high-temperature applications.

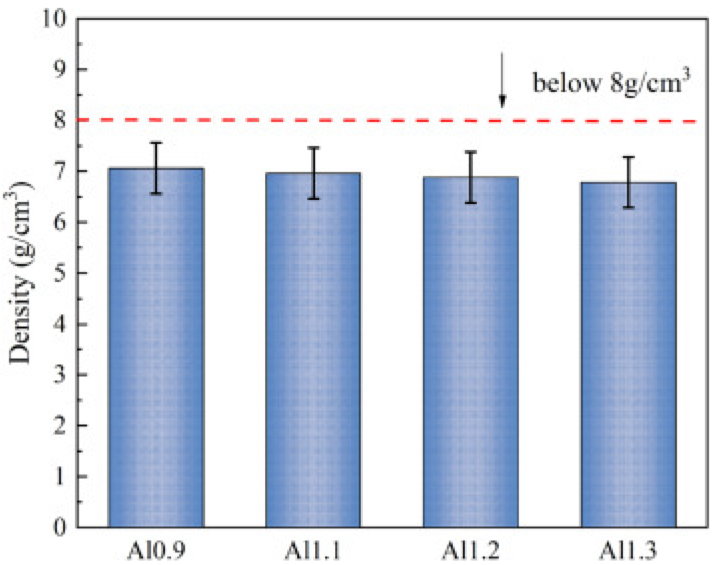

1. Download: Download high-res image (499KB)
2. Download: Download full-size image

Fig. 2. Density of theFe2Ni2CrAlx MPEAs.

To measure the melting point, Fig. 3 shows the DSC curves of the Fe2Ni2CrAlx MPEAs with the temperature ranging from 30 °C to 1500 °C. All the alloys exhibit similar characteristics, an endothermic peak occurred at the end of the curves which represents melting. It can be observed that a narrow temperature interval existed between the solidus and liquidus temperatures. Some typical physical characteristics, e.g., the initial melting temperature (Ts), final melting temperature (Tf) were summarized in Table 1. The Fe2Ni2CrAl0.9 MPEA began to melt at 1317.7 °C and completed melting at 1362.7 °C. As the atomic ratio of Al increases to 1.1, a slight increase of Ts can be observed from 1317.7 °C to 1317.9 °C, the Tf significantly increased from 1362.7 °C to 1371.0 °C. Thus the Ts and Tf of Fe2Ni2CrAlx MPEAs increases by greater Al addition. Accordingly, the addition of Al contributes to the melting point of Fe2Ni2CrAlx MPEAs. Fe2Ni2CrAl1.3 MPEA has the highest melting point, with Ts of 1337.7 °C and Tf of 1392.6 °C. Notably, there is no any phase transition below 1300 °C since no endothermic peak was found until melting.

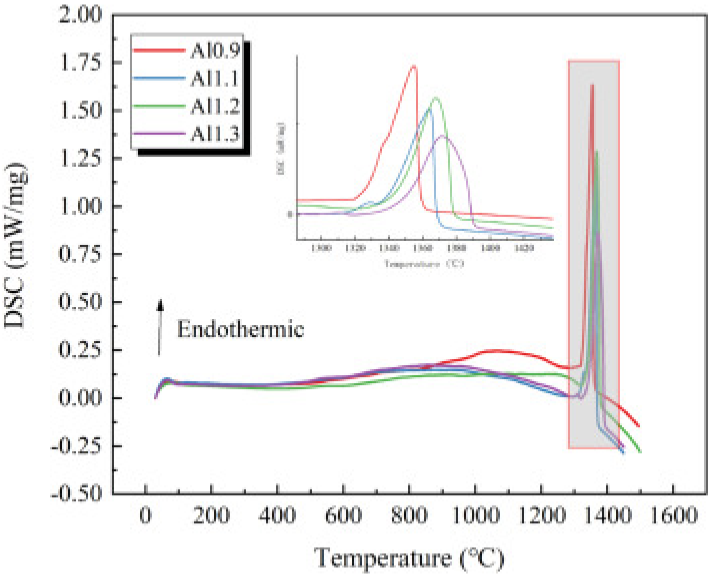

1. Download: Download high-res image (242KB)
2. Download: Download full-size image

Fig. 3. DSC patterns of theFe2Ni2CrAlx MPEAs.

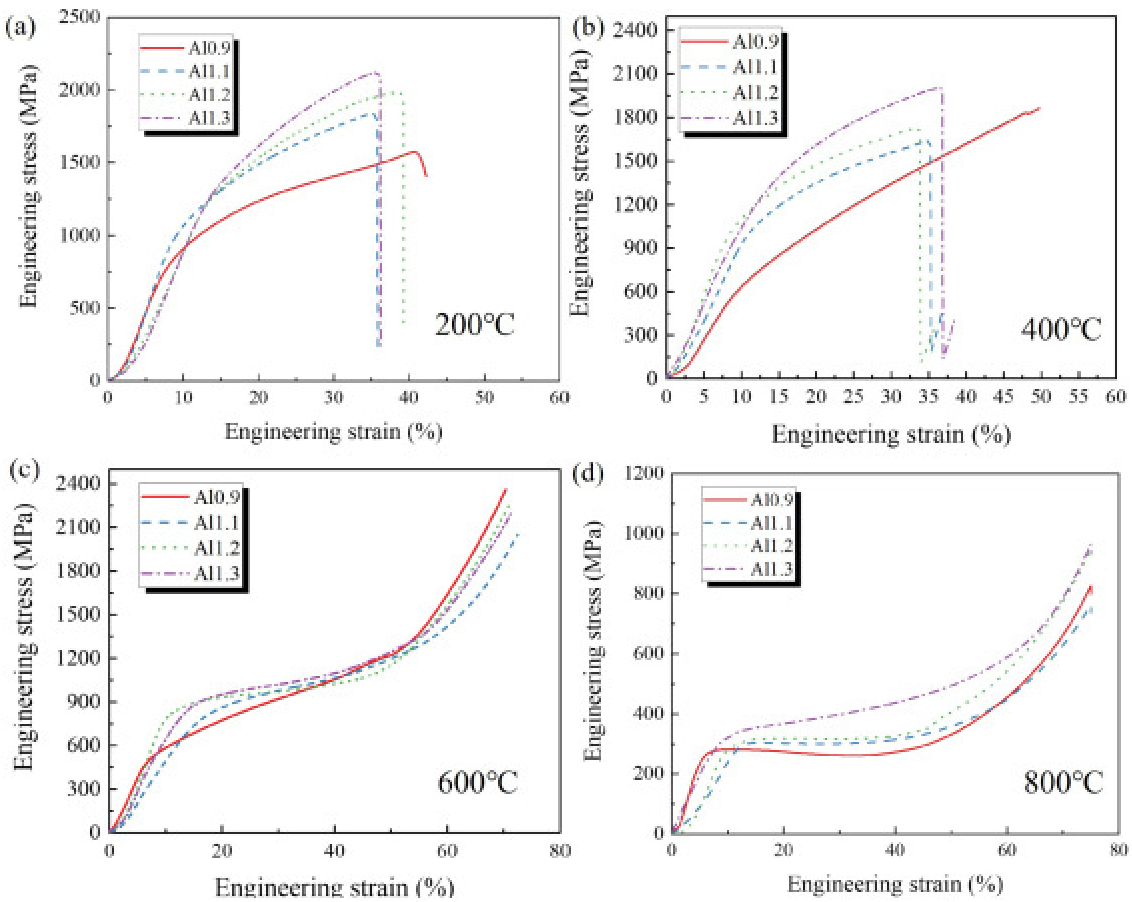

1. [Download: Download high-res image (590KB)]
2. [Download: Download full-size image]

Fig. 4. Engineering stress–strain curves of Fe2Ni2CrAlx MPEAs at elevated temperature (a) 200 °C (b) 400 °C (c) 600 °C (d) 800 °C.

Table 1. DSC results of Fe2Ni2CrAlx MPEAs.

MPEAs	Ts (°C)	Tf (°C)
Al0.9	1317.7	1362.7
Al1.1	1317.9	1371.0
Al1.2	1327.4	1380.8
Al1.3	1337.7	1392.6

3.3. High temperature mechanical properties

Compression Tests: Fig. 4 shows the compressive stress–strain curves of Fe2Ni2CrAlx MPEAs under the testing temperatures ranging from 200 °C to 800 °C. It is evident that the strength gradually decreases with rising temperature. At 200 °C, the fracture strength of Fe2Ni2CrAl0.9 MPEA is 1572 MPa, with plastic strain of 40.7%. When the atomic ratio of Al increases to 1.1, the strength increases to 1836 MPa, accompanied by a reduction of plastic strain to 34.8%. By the successive Al addition, the fracture strength increased to 1981 MPa and 2119 MPa for the Fe2Ni2CrAl1.2 MPEA and Fe2Ni2CrAl1.3 MPEA, respectively. When the temperature increased to 400 °C, a significant enhancement can be observed in plasticity for the Fe2Ni2CrAl0.9 MPEA. When the atomic ratio of Al exceeds 1.1, a slight reduction of strength was acquired. The fracture strength of Fe2Ni2CrAl1.1 MPEA and Fe2Ni2CrAl1.2 MPEA was 1642 MPa and 1722 MPa, respectively, both exceeding 1500 MPa. As the atomic ratio of Al reached 1.3, the fracture strength can achieve 2003 MPa, with the plastic strain of 36.4%. It is surprising that Fe2Ni2CrAl1.3 MPEA attained such high strength without compromising plasticity. With the temperature rising to 600 °C and 800 °C, no fracture occurred even until a compressive strain above 70%, which suggests that the developed Fe2Ni2CrAlx alloys exhibit an exceptional high-temperature compressive plasticity. While, when it reaches a large deformation (>50%) at 600 °C and 800 °C, the effective contact area does not match the recognized contact area of the equipment, resulting in a larger experimental deviation for the increase in engineering stresses in the final section of the stress–strain curves. The alloy with high Al contents, especially Fe2Ni2CrAl1.3 MPEA, have the benefit of sustained high strength and extended plasticity at elevated temperatures, which were superior to most HEAs and was even comparable with Ti-based alloys (Ti-6Al-4V-0.1B, Ti-10V-2Fe-3Al) [44], [45].

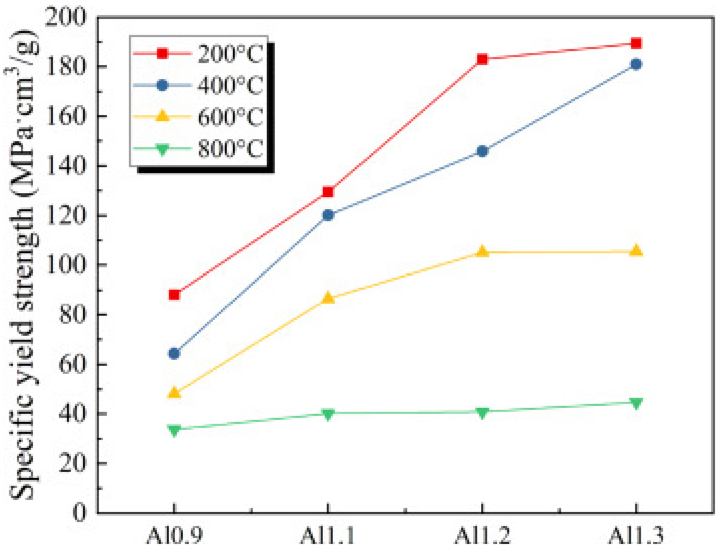

1. Download: Download high-res image (194KB)
2. Download: Download full-size image

Fig. 5. Specific yield strength of Fe2Ni2CrAlx MPEAs.

Temperature dependence of SpecificYield Strength: Fig. 5 plotted the temperature dependence of the specific yield strength of Fe2Ni2CrAlx MPEAs. It was evident that with a rise in temperature, there was an obvious decrease in specific yield strength. The specific yield strength of Fe2Ni2CrAl0.9 MPEA gradually decreased from 88.2 MPa·cm3/g at 200 °C to 64.3 MPa·cm3/g at 400 °C, and then dropped to 48.2 MPa·cm3/g and 33.7 MPa·cm3/g at 600 °C and 800 °C, respectively. Once the atomic ratio of Al surpassed 1.1, increases in specific yield strength became apparent at temperature below 600 °C. At 200 °C and 400 °C, the specific yield strength of Fe2Ni2CrAl1.1 MPEA increased to 129.5 MPa·cm3/g and 120.1 MPa·cm3/g, respectively. While, when the temperature rises to 600 °C, the upward trend of increase has decelerated, and slowed down even further at 800 °C. Fe2Ni2CrAl1.2 MPEA exhibits much higher specific yield strength than Fe2Ni2CrAl1.1 MPEA. Due to the low-density element Al, the density of alloys tended to further decrease with the addition of Al and Fe2Ni2CrAl1.3 MPEA possessed the lowest density. Thus, the Fe2Ni2CrAl1.3 MPEA maintained the highest specific yield strength at elevated temperature. Fe2Ni2CrAl1.3 MPEA shows the specific yield strength of 189.5 MPa·cm3/g at 200 °C, and even above 105.5 MPa·cm3/g as the temperature increased to 600 °C. With the temperature of 200~400°C, there is no obvious softening existing in the alloy, thus the Fe2Ni2CrAl1.3 MPEA also has great specific yield strength. However, with a further increase of temperature (600~800°C), it presents a decline in the specific yield strength of the Fe2Ni2CrAl1.3 MPEA despite it still exhibiting a higher level compared with other reported alloys [43]. Even at 800 °C, the present alloy exhibits the highest specific yield strength among the investigated alloys, suggesting exceptional softening resistance at high temperature.

Fracture Studies: To study the fracture modes, the fracture surfaces of failed Fe2Ni2CrAlx MPEAs were examined. After compression at 200 °C, Fe2Ni2CrAlx (x = 1.1, 1.2, 1.3) MPEAs were completely fractured, the fractographic features were presented in Fig. 6. For all deformed samples, obvious torn edges can be found on the fracture surface. From Fig. 6 (a1) and (a2), cleavage and quasi-cleavage features manifest on the fracture surfaces of Fe2Ni2CrAl1.1 MPEA under uniaxial compression. Fig. 6 (a2) showed a small part of shallow dimple patterns. Fig. 6 (b1)–(b2) showed cleavage steps on the fracture surface of Fe2Ni2CrAl1.2 MPEA. For Fe2Ni2CrAl1.3 MPEA, Fig. 6 (c1) showed typical characteristic of bright island-like facets surrounded by and river-like patterns on the fracture surface. The facets are characteristic of cleavage fracture patterns, and the formation of river-like patterns are attributed to the merging of cleavage steps within a single grain. Fig. 6 (c2) showed gray slip lines, due to slip driven by shear stress. As the temperature increases to 400 °C, only Fe2Ni2CrAl1.3 MPEA is completely fractured, fractographic features were given in Fig. 6 (d1) and (d2). Cleavage steps and slip lines were found on the fracture surfaces. Accordingly, the fracture mechanism of Fe2Ni2CrAlx MPEAs can be classified as a combination of cleavage and slip separation, indicating that brittle fracture occurred under compression.

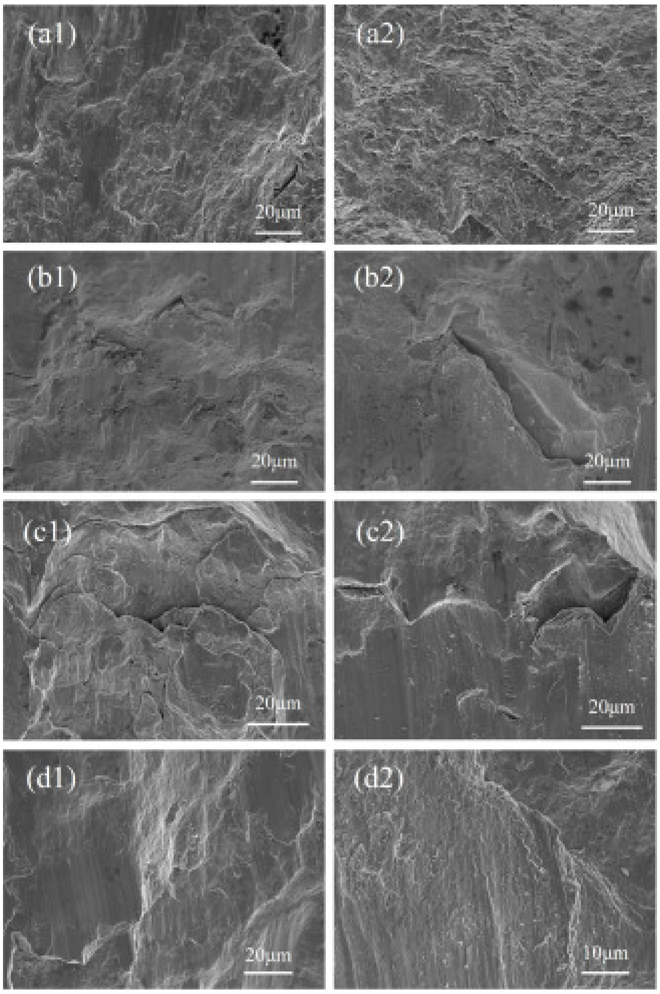

1. Download: Download high-res image (935KB)

2. Download: Download full-size image

Fig. 6. Fractographic features of (a1)(a2) Al1.1 (b1)(b2) Al1.2 (c1)(c2) Al1.3 at 200 °C; Fractographic features of (d1)(d2) Al1.3 at 400 °C.

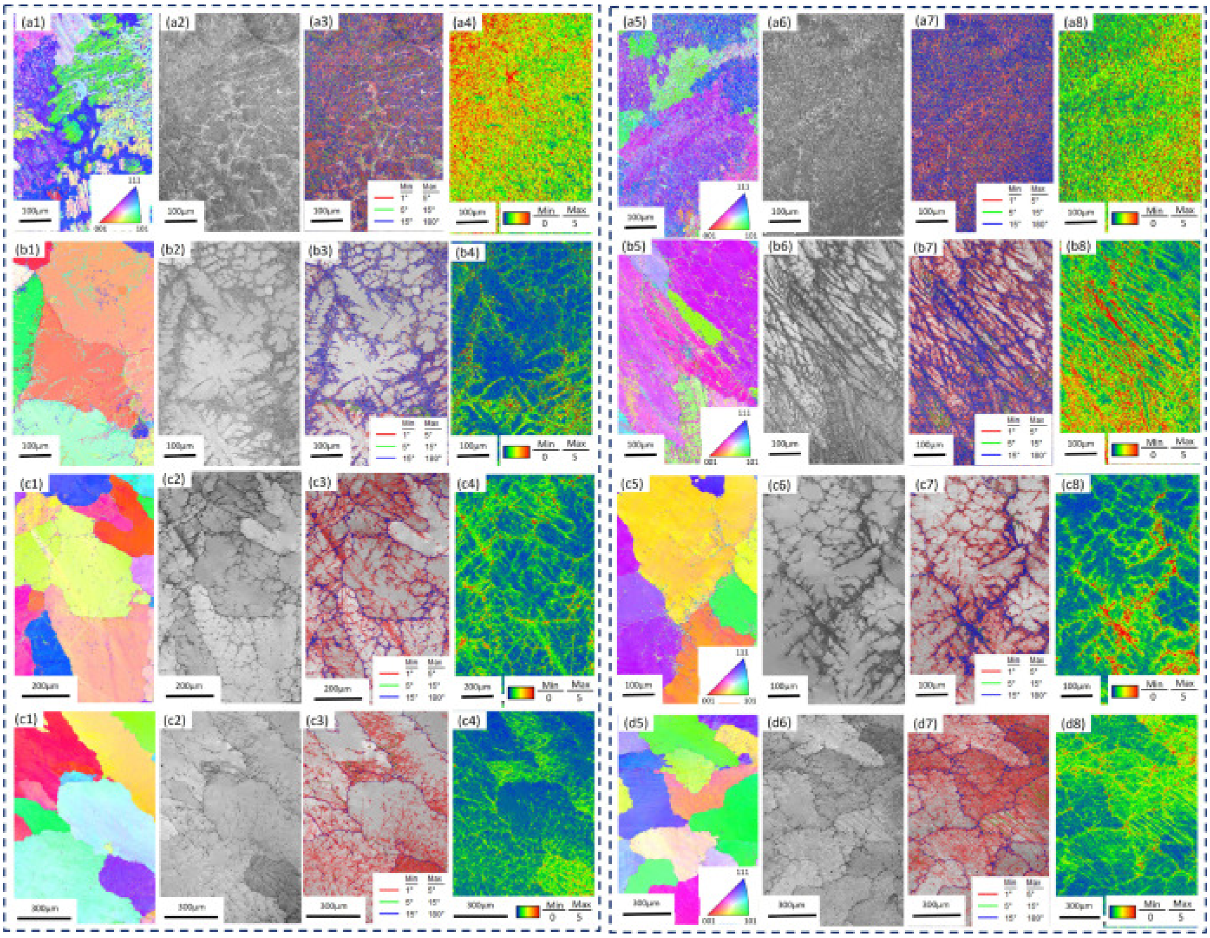

1. Download: Download high-res image (5MB)
2. Download: Download full-size image

Fig. 7. EBSD results on the deformed sample at 200 °C: (a1)–(a4) Al0.9 (b1)–(b4) Al1.1 (c1)–(c4) Al1.2 (d1)–(d4) Al1.3 and 400 °C: (a5)–(a8) Al0.9 (b5)–(b8) Al1.1 (c5)–(c8) Al1.2 (d5)–(d8) Al1.3. (For interpretation of the references to color in this figure legend, the reader is referred to the web version of this article.)

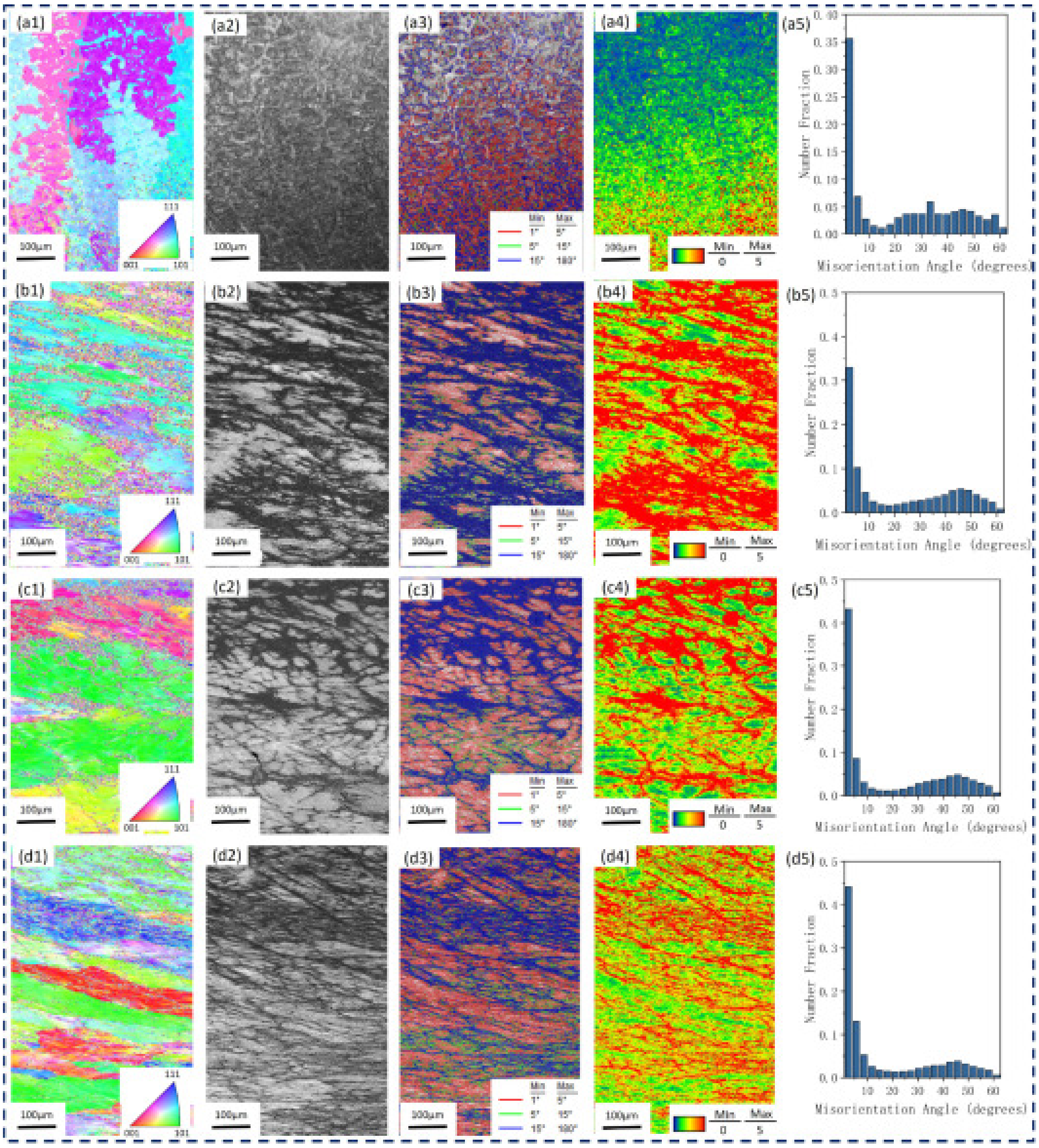

1. [Download: Download high-res image (3MB)]
2. [Download: Download full-size image]

Fig. 8. EBSD results on the deformed sample at 600 °C (a1)–(a5) Al0.9 (b1)–(b5) Al1.1 (c1)–(c5) Al1.2 (d1)–(d5) Al1.3.

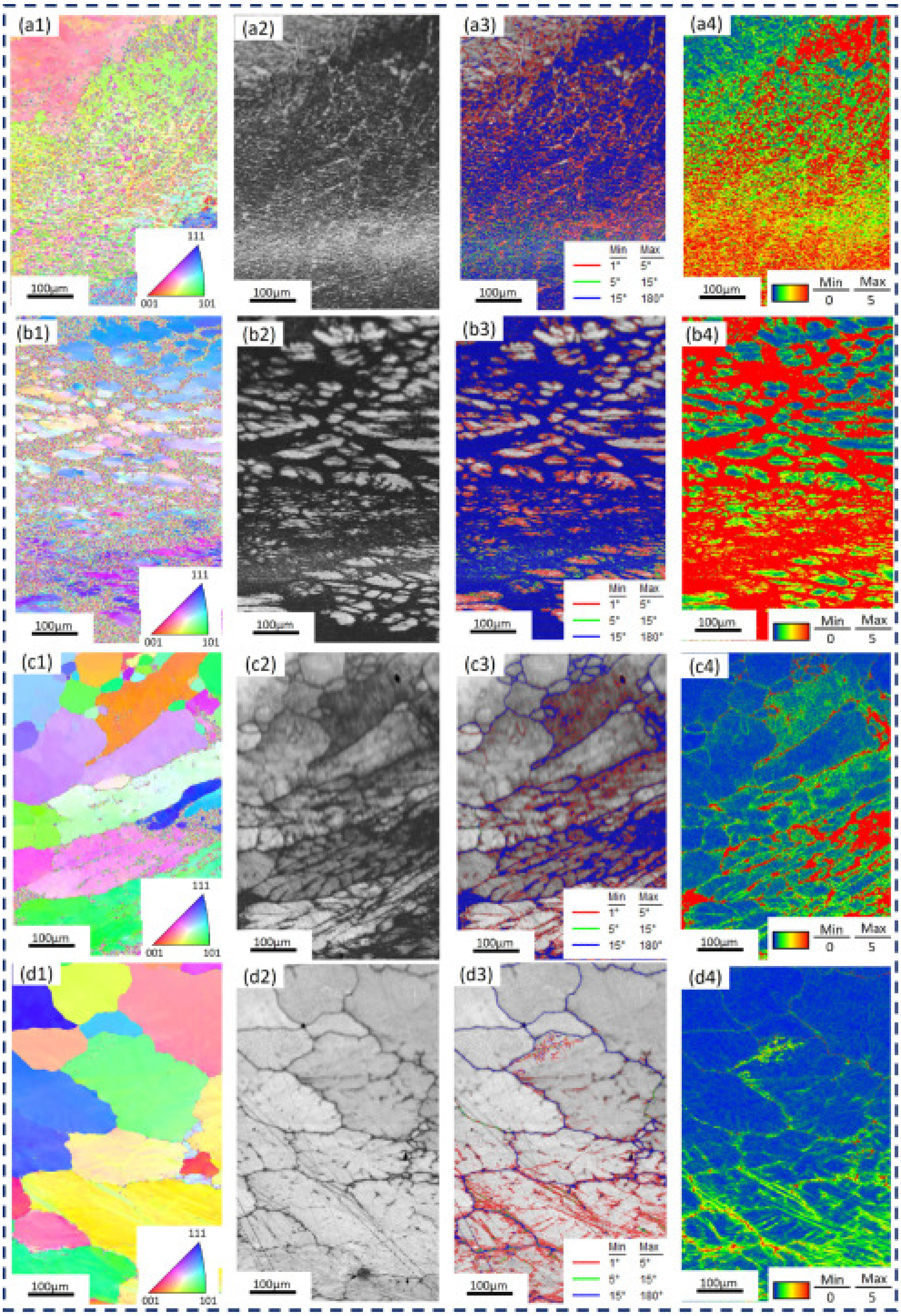

1. [Download: Download high-res image (3MB)]
2. [Download: Download full-size image]

Fig. 9. EBSD results on the deformed sample at 800 °C (a1)–(a5) Al0.9 (b1)–(b5) Al1.1 (c1)–(c5) Al1.2 (d1)–(d5) Al1.3.

EBSD of Deformed Samples: To further understand the deformation behavior of Fe2Ni2CrAlx MPEA, Fig. 7 showed the EBSD results on the deformed sample at 200 °C and 400 °C. After the deformation at 200 °C, the IPF and corresponding IQ maps were presented in Fig. 7 (a1)–(d1) and (a2)–(d2). In accordance with the legend depicted in Fig. 7 (a1)–(d1), the orientations of [001], [101], and [111] were denoted by red, blue, and green, respectively. The varied colors on the IPF map represented a random crystallographic texture. Fe2Ni2CrAl0.9 MPEA exhibited typical dendritic morphology. As the atomic ratio of Al increases to above 1.1, the grains showed equiaxial shape and slightly elongated grains in some regions. Grain boundaries are divided into low angle grain boundaries (LAGBs) and high angle grain boundaries (HAGBs). The grain boundary (GB) maps were plotted in Fig. 7 (a3)–(d3). Obvious HAGBs were captured in Fe2Ni2CrAl0.9 and Fe2Ni2CrAl1.1 MPEA. While, a large number of sub-boundary were observed in Fe2Ni2CrAl1.2 and Fe2Ni2CrAl1.3 MPEA. Fig. 7 (a4)–(d4) illustrated the KAM maps on the deformed sample, which showed higher KAM values compared to the initial microstructure. KAM maps for various regions showed different local strain levels. The grain boundary was predominantly red, the area within the grains were green. It demonstrated a high KAM value for the grain boundary and a lower KAM value within the grains. Accordingly, the plastic deformation was more severe at the boundary, resulting in the non-uniform strain distribution during compression.

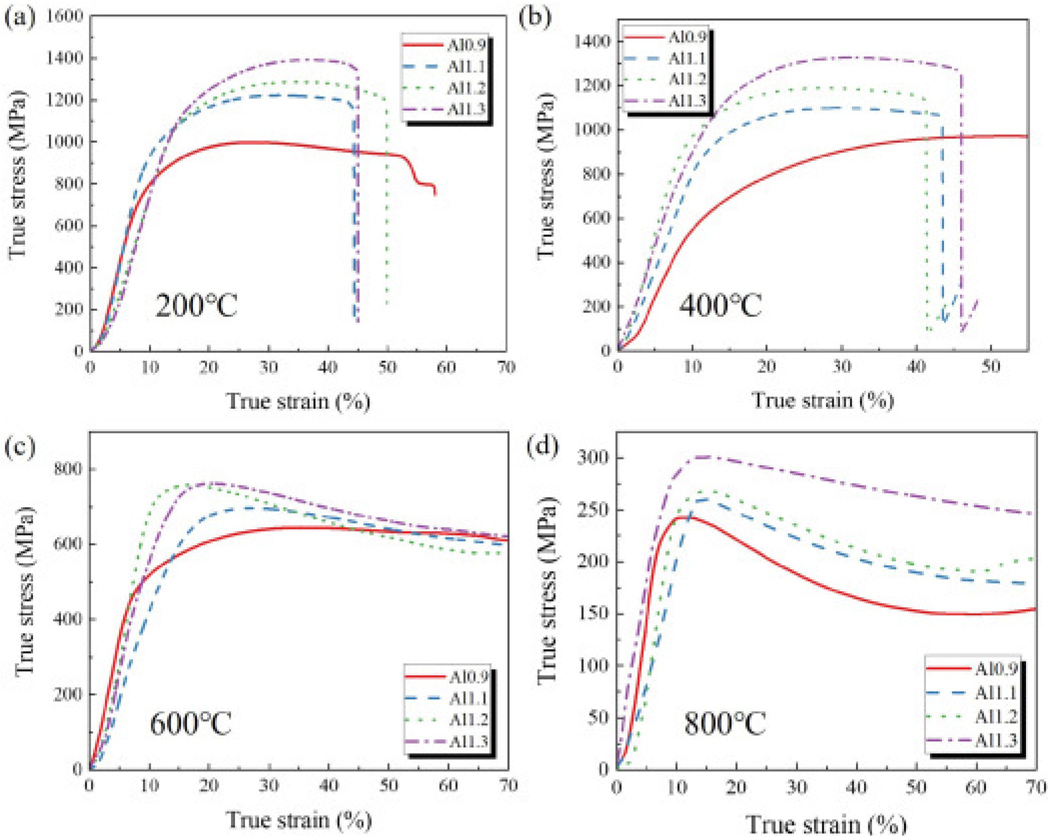

1. Download: Download high-res image (545KB)
2. Download: Download full-size image

Fig. 10. True stress–strain curves of Fe2Ni2CrAlx MPEAs at elevated temperature (a) 200 °C (b) 400 °C (c) 600 °C (d) 800 °C.

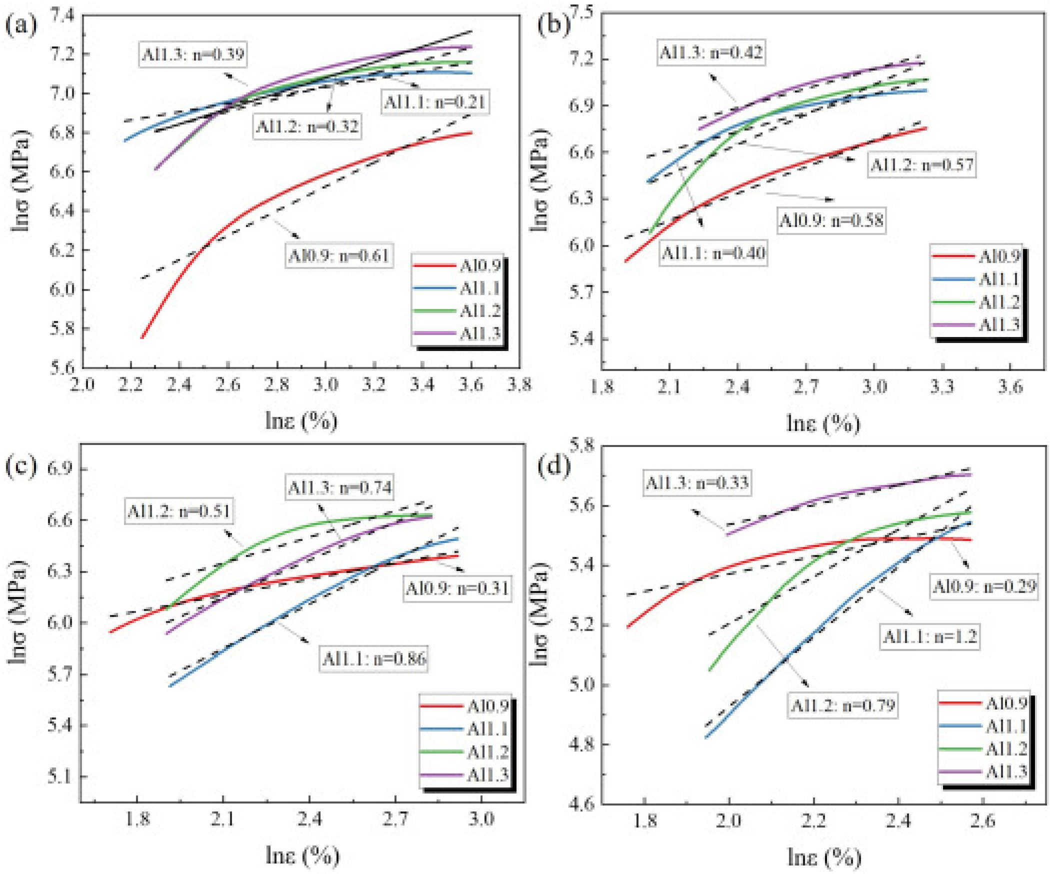

1. Download: Download high-res image (611KB)
2. Download: Download full-size image

Fig. 11. The relationship of εlnε−lnσ and the corresponding fitted curves (a) 200 °C (b) 400 °C (c) 600 °C (d) 800 °C.

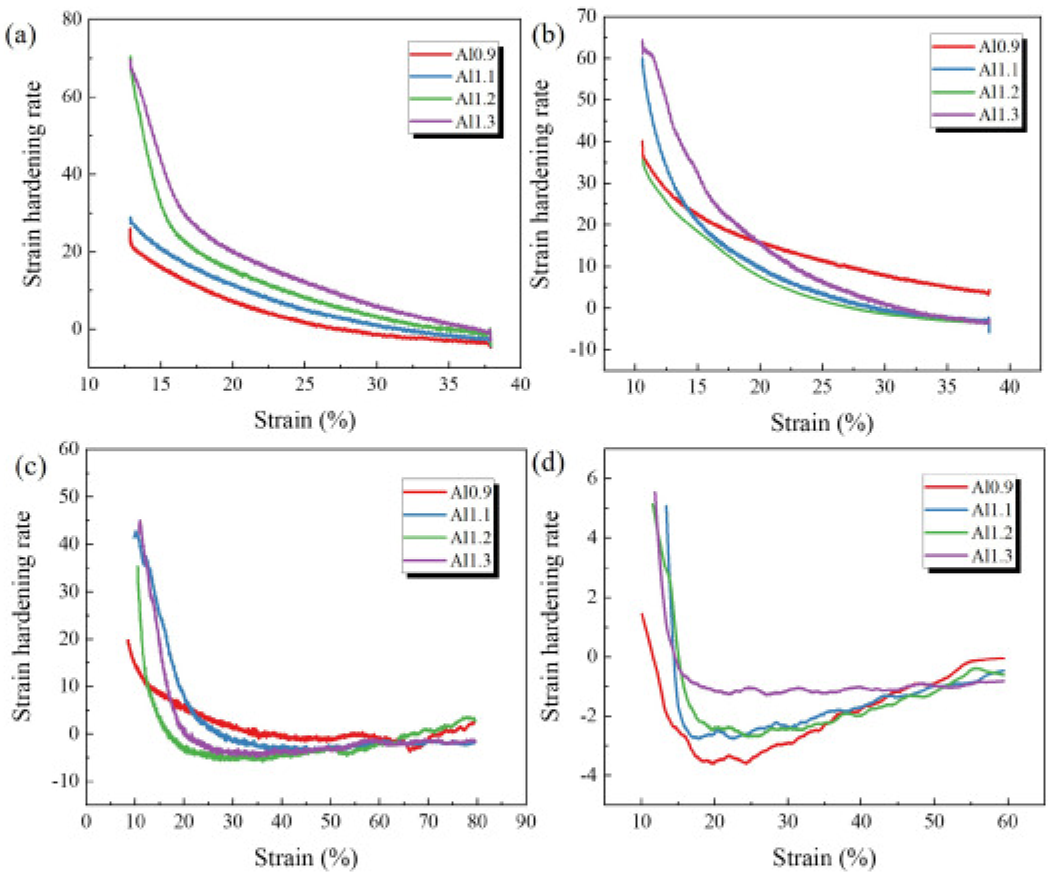

1. Download: Download high-res image (538KB)
2. Download: Download full-size image

Fig. 12. Strain hardening rate of Fe2Ni2CrAlx MPEAs at elevated temperature (a) 200 °C (b) 400 °C (c) 600 °C (d) 800 °C.

Fig. 7 (a5)–(d5) and (a6)–(d6) the IPF and corresponding IQ maps of the deformed sample after compression at 400 °C. The increase in grain size in the Fe2Ni2CrAl0.9 MPEAs (Fig. 7 (a5)) was detected in comparison to the deformed microstructure at 200 °C. Hence, at the same deformation degree, the grain size tends to increase as the deformation temperature rises. From Fig. 7 (b5) and (b6), a large number of elongated grains can be observed in Fe2Ni2CrAl1.1 MPEAs, which was quite different from that at deformation temperature of 200 °C. Similar with the deformation at 200 °C, the interior of grains contained a lot of LAGBs (Fig. 7 (a7)–(d7)) and in general the overall misorientation within the grains slightly increased (Fig. 7 (a8)–(d8)). Based on our results, any noticeable porosity on the microstructure evolution during compression was not revealed.

Fig. 8 presented the EBSD results on the deformed sample at 600 °C. From Fig. 8 (a1)–(d1) and (a2)–(d2), the IPF and IQ maps showed the formation of a lamellar-type microstructure with lamellae elongated along the direction of metal flow. In some areas, small recrystallized grains appearing, especially when the atomic ratio of Al is above 1.1, indicating the recrystallization softening at high-temperature. Owing to the transformation of coarse equiaxed grains into subgrains during plastic deformation, the microstructure was fragmented by crossing microshear bands and a number of LAGBs formed in the grains (Fig. 8 (a3)–(d3)). Fig. 8 (a4)–(d4) illustrated the KAM maps on the deformed sample, which showed higher KAM values compared to the deformed microstructure at 200 °C and 400 °C. The misorientation angle distribution were summarized in Fig. 8 (a5)–(d5), the overall misorientation at the same temperature changed considerably with varying Al contents. More LAGBs can be found within the grains as the atomic content of Al exceeds 1.2. The observed inhomogeneous microstructure was probably associated with non-uniform strain distribution during compression. The grain-boundary strengthening resulted in the superior strength of Fe2Ni2CrAl1.2 MPEAs and Fe2Ni2CrAl1.3 MPEAs.

The EBSD results on the deformed sample at 800 °C were presented in Fig. 9. From Fig. 9 (a1) and (a2), the recrystallization softening occurred in Fe2Ni2CrAl0.9 MPEAs. Very fine equiaxed grains can be detected at dendrite boundaries. A lot of subgrain boundaries are generated within the dendrites (Fig. 9 (a3)), exhibiting large misorientation with high KAM values (Fig. 9 (a4)). For the Fe2Ni2CrAl1.1 MPEAs (Fig. 9 (b1)–(b4)), shear bands were observed to coincide with initial grain boundaries, substructures were developed with high KAM value. Compared with that at 600 °C, the increase in deformation temperature to 800 °C resulted in the increase of the size of new grains in Fe2Ni2CrAl1.2 MPEAs (Fig. 9 (c1) and (c2)). The small equiaxed grains rose due to the development of dynamic recrystallization in severely deformed regions. Some shear bands within the grains were inclined predominantly at ~45° to compression direction. The elongated subgrains were observed in the initial coarse grains. Subgrains with LAGBs were shown in Fig. 9 (c3), and it showed large misorientation in subgrains. From Fig. 9 (d1) and (d2), the formation of almost completely recrystallized structure was identified in Fe2Ni2CrAl1.3 MPEAs. The size of the recrystallized grains increased noticeably at 800 °C. The number of GBs was reduced, as well as the overall KAM value (Fig. 9 (d3) and (d4)). At higher temperatures, both grain strength and grain boundary strength decrease, whereas the decrease in grain boundary strength is faster than grains. Thus, the developed Fe2Ni2CrAl1.3 MPEAs exhibited superior strength and plasticity at 800 °C. Dynamic recrystallization also helps in relieving internal stresses caused by deformation, improving the overall stability and integrity of the Fe2Ni2CrAl1.3 MPEAs.

With respect to the microstructural analysis, no structural changes were observed for the developed Fe2Ni2CrAlx MPEAs after high temperature deformation. Cracks were not observed at all the tested temperatures. The obvious coarsening was observed in samples deformed at higher temperatures, whereas the microstructure is still lamellar in appearance in Fe2Ni2CrAl0.9 MPEAs and retained polygonal grain in Fe2Ni2CrAlx MPEAs (x>1.1). Regarding the typical high-temperature alloys, the significant coarsening and loss of lamellar morphology were observed in AlCoCrFeNi2.1 HEAs [46] and a large amount of intragraunlar η precipitates formed a Widmanst tten pattern in the INCONEL alloy 740 [47] at high temperature. Hence, the microstructural stability of Fe2Ni2CrAlx MPEAs is comparable with the typical high-temperature alloys [46], [47]. During high-temperature deformation, dynamic recrystallization is indeed a crucial mechanism in controlling the evolution of the microstructure for various metals and alloys [48]. The recrystallized fraction in deformed samples depends on the temperatures. At high temperatures, the recrystallized fraction generally increases. For Fe2Ni2CrAlx MPEAs, subgrains develop in the vicinity of grain boundaries, and as deformation increases, subgrain formation spreads throughout the entire grain volume. This phenomenon can also be observed in other typical high-temperature alloys, such as CoCrFeNiMn and FeCoNiMnV HEAs [49], [50], Ti-6.8Mo-4.5F-1.5Al [51] and nickel-based superalloy [52]. It suggests the development of dynamic recrystallization in the alloy during the deformation at elevated temperatures. The progressive increase in misorientation of existing subboundaries eventually converts them into HAGBs [53], [54].

3.4. Work-hardening behavior at elevated temperatures

Fig. 10 plotted the true stress–strain curves of Fe2Ni2CrAlx MPEAs at elevated temperature. Under true stress–strain conditions, the strength of Fe2Ni2CrAl1.3 MPEA were 1392 MPa and 1328 MPa at 200 °C and 400 °C, respectively. After yielding, all the studied alloys showed continuous strengthening. With an increase in the testing temperature to 600 °C, a decrease in the yield strength was identified and resulted in a reduced work hardening. It indicated that the work hardening capability of the Fe2Ni2CrAlx MPEAs can be retained up to 800 °C. The alloys exhibited a very short work hardening stage after yielding, followed by a steady state flow stage. It should be noted that the decrease in true stresses are observed in the steady state flow stage at 600 and 800 °C. This is due to the softening process caused by dynamic recrystallization at high temperature.

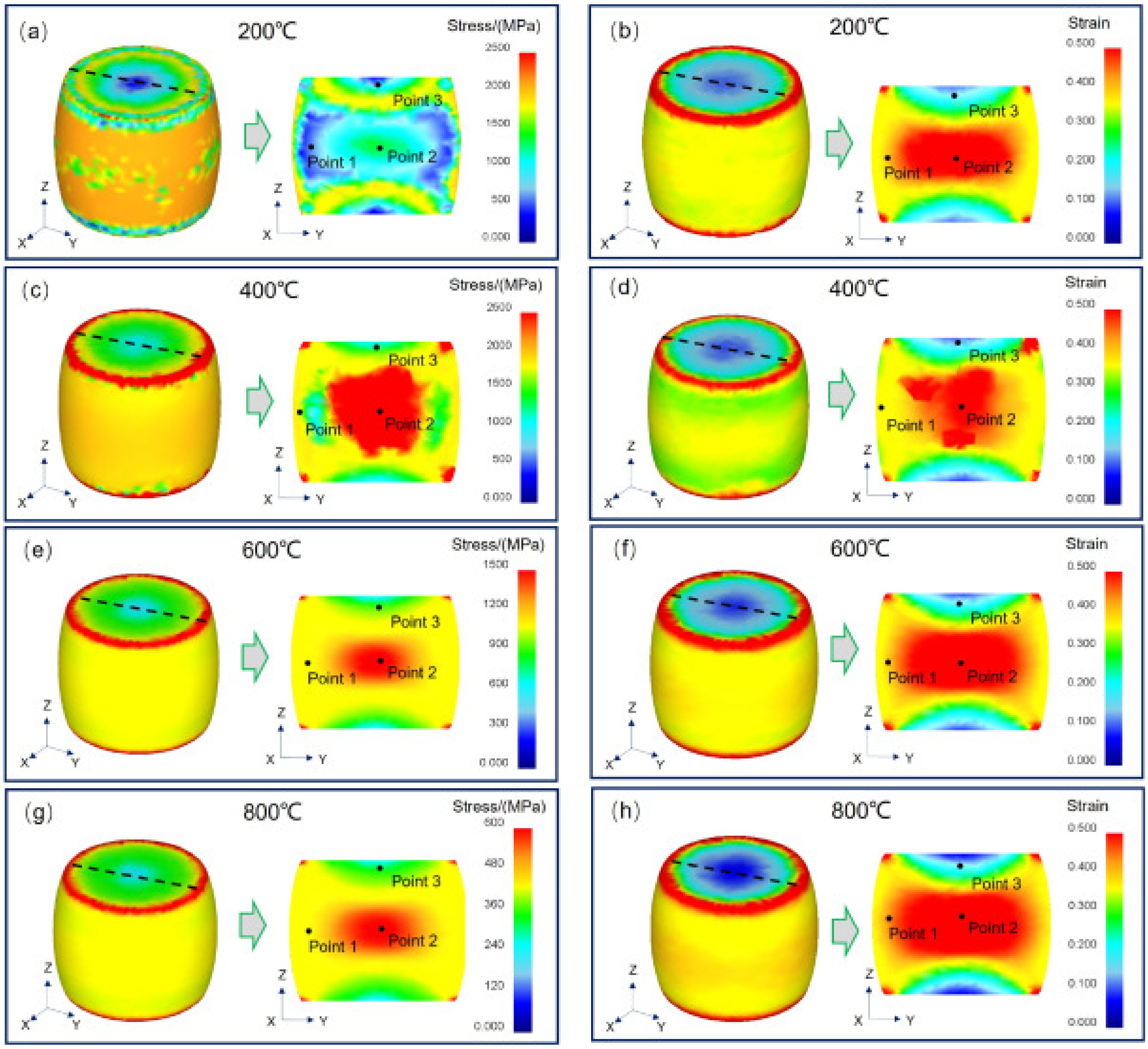

1. Download: Download high-res image (1MB)
2. Download: Download full-size image

Fig. 13. Distribution of stress–strain field during deformation process at elevated temperature (a)(b) 200 °C (c)(d) 400 °C (e)(f) 600 °C (g)(h) 800 °C.

The mechanical behavior was also assessed particularly focusing on its work hardening capability. Hollomon analysis was utilized on the true stress–strain data during the plastic deformation to investigate the hardening behavior of Fe2Ni2CrAlx MPEAs at elevated temperatures, as expressed in Eq. (1) [55](1) $\varepsilon\sigma=k\varepsilon n$ where, k denotes the strength coefficient, n denotes the hardening exponent. In general, n is a critical parameter that significantly influences the strain coordination capacity of materials. A higher n indicates a material that can sustain higher levels of plastic deformation before failure, demonstrating better strain coordination capacity.

Fig. 11 plotted the relationship of $\varepsilon \ln\varepsilon - \ln\sigma$ and the corresponding fitted curves during plastic deformation process after yielding. The $\varepsilon \ln\varepsilon - \ln\sigma$ plots at various temperature were close to a linear relationship. At 200 °C, the Fe2Ni2CrAl0.9 MPEA showed a n value of 0.61, then dropped to 0.21 for Fe2Ni2CrAl1.1 MPEA. With an increase in Al content from 1.2 to 1.3, the n increased from 0.32 to 0.39. As the temperature rose to 400 °C, Fe2Ni2CrAl0.9 MPEA and Fe2Ni2CrAl1.2 MPEA possessed stronger work hardening effect, with n value of 0.58 and 0.57, respectively. At 600 °C, Fe2Ni2CrAl1.1 and Fe2Ni2CrAl1.3 MPEA possessed a higher n value of 0.86 and 0.74, respectively. With a further increase in temperature to 800 °C, the n value of Fe2Ni2CrAl1.3 MPEA decreased to 0.33. A slight variation can be observed for the Fe2Ni2CrAl0.9 MPEA, with the n value of 0.29. The n value of Fe2Ni2CrAl1.1 MPEA and Fe2Ni2CrAl1.2 MPEA are much higher than Fe2Ni2CrAl0.9 MPEA and Fe2Ni2CrAl1.3 MPEA. In general, during plastic deformation, the grain slip leads to entanglement of dislocations, elongation, fragmentation, and fibrosis of the grains, and residual stresses are generated inside the alloys. Due to the excellent plasticity of Fe2Ni2CrAl0.9 MPEAs at 200 °C and 400 °C, compared with other alloys, it shows the most desirable strain coordination capacity. As temperature increases to 600 °C and 800 °C, all the developed alloys display great plasticity. The nucleation of new grains and the consumption of old grains through dynamic recrystallization create a fine-grained microstructure that impedes dislocation motion, allowing a good strain coordination capacity of Fe2Ni2CrAl1.1 MPEA.

For a further understanding, the work-hardening behavior of Fe2Ni2CrAlx MPEA can be evaluated by the strain-hardening rate θ, as expressed in Eq. (2) [56].(2)$\varepsilon\theta = d\sigma/d\varepsilon$where σ denotes the true stress and εε corresponds to the strain. Based on the true stress–strain curves, θ can be obtained as a function of true plastic strain, as illustrated in Fig. 12. From the plot, a rapid drop was observed in the initial stage of the curves. With an increase of true strain, the θ curves displayed an almost linear reduction at the temperature of 200 °C and 400 °C. As the temperature rises to 600 °C and 800 °C, the Fe2Ni2CrAlx MPEAs undergo softening during deformation, and as the strain increases, the work hardening behavior and softening mechanism reach a dynamic equilibrium, with the θ curves tending to stabilize. The θ increased with the addition of Al at 200 °C and 800 °C. While, at 400 °C and 600 °C, Fe2Ni2CrAl0.9 MPEAs displayed a higher θ in the steady state.

Accordingly, the Fe2Ni2CrAlx (x>1.1) MPEA exhibited superior high-temperature strengths up to 800 °C; the Fe2Ni2CrAl1.3 MPEA, especially, had exceptional plasticity and a large strain-hardening capacity, and is a very promising candidate for high-temperature service. The formation and evolution of subgrains contribute to continuous strain hardening. HAGBs can act as effective barriers to dislocation motion and promote work-hardening ability. According to the EBSD analysis on the initial microstructure, there is no simple relationship between the grain size and mechanical properties at elevated temperature.

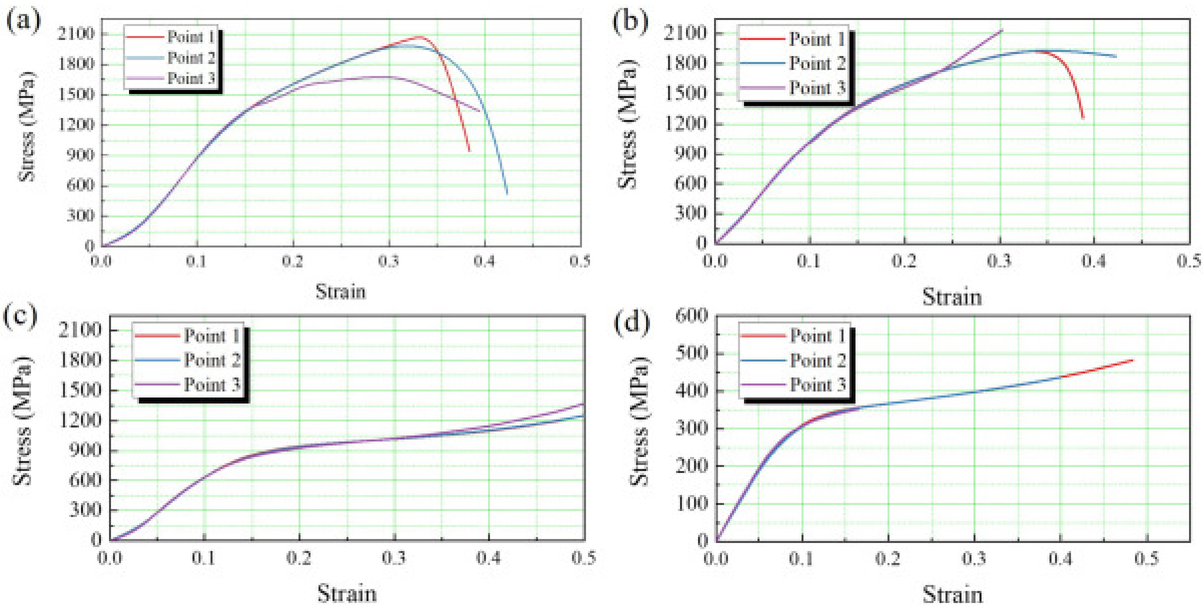

1. Download: Download high-res image (724KB)
2. Download: Download full-size image

Fig. 14. Stress–strain curves obtained from FEM simulation (a) 200 °C (b) 400 °C (c) 600 °C (d) 800 °C.

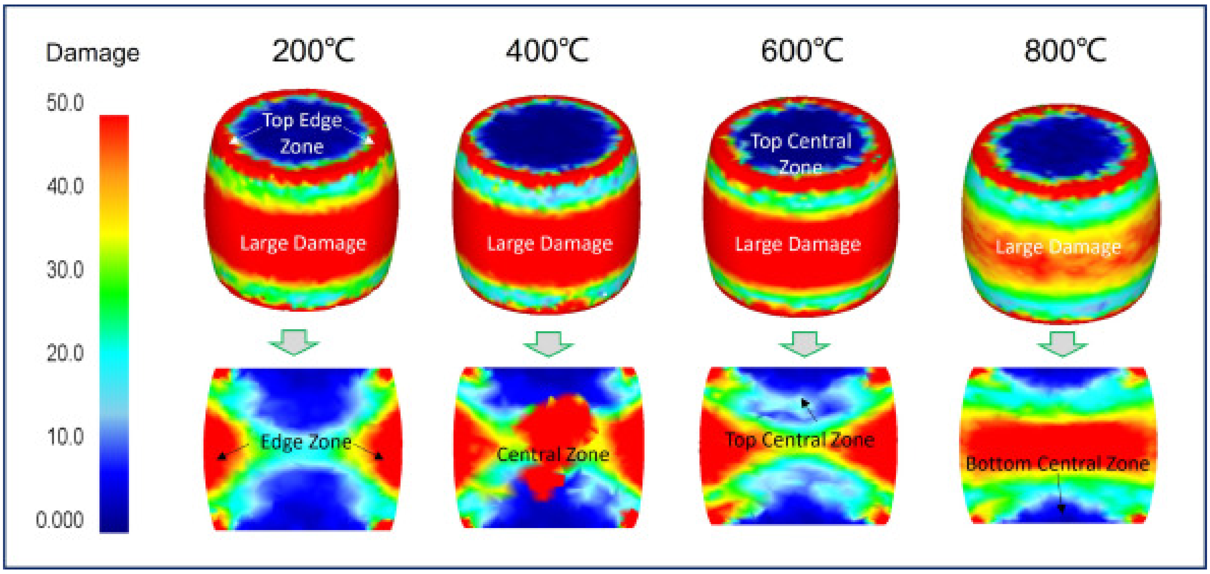

1. Download: Download high-res image (640KB)
2. Download: Download full-size image

Fig. 15. Distribution of damage field during deformation process at elevated temperature.

3.5. Finite element simulation on deformation behavior at elevated temperatures

The deformation behavior of Fe2Ni2CrAl1.3 MPEA was simulated using a FEM simulation package at various temperature (200 °C, 400 °C, 600 °C, 800 °C). The upper die is moving down while the lower die remains stationary, which was consistent with the process of compression test. Fig. 13 depicted the resulting contour map for the distribution of stress field and the corresponding strain field within the sample. Herein, Fig. 13 (a)(b) and (c)(d) illustrated the state of sample before fracture at 200 °C and 400 °C, respectively. Since no fracture occurred above 400 °C, Fig. 13 (e)(f) and (g)(h) presented the state of sample after undergoing a 50% deformation. It can be observed that the stress and strain field within the sample varied with the temperatures. At all temperature conditions, Fe2Ni2CrAl1.3

MPEA experienced significant strain at the center. From the perspective of the top view, the top central zone exhibited small stress and strain since the flowability was reduced in the contact areas resulted from expected friction effects. The FEM simulations effectively demonstrated the inhomogeneity within the sample, stress concentration and the highest strain occurring at the center of the sample.

To further investigate the mechanical evolution within the sample under compressive load, we selected 3 typical points, located at the position near the edge in the middle of the sample (point 1), the centeral position in the middle of the sample (point 2), and the central zone near the top die (point 3). Fig. 14 showed the comparison of the stress–strain at the 3 points simulated by the FEM simulation at different temperatures. From Fig. 14 (a), there were significant differences in stress–strain evolution among the three points in the deformed sample. It can be inferred that the deformation within the sample is uneven under compression at 200 °C. The stress at point 3 was significantly smaller than the points at interior of the sample. As the temperature increases, the stress–strain curves of the three points were nearly overlapping. Evidently, the deformation inside the sample became more uniform when the temperature exceeds 400 °C, only slight differences can be observed. For comparison, the evolution trend of the stress–strain curve obtained from simulation were consistent with the curve measured from experiments, verifying the reliability of the FEM simulation results.

To understand the degree of damage to the sample under compressive load, Fig. 15 presented the distribution of damage field during deformation process at elevated temperature. Obviously, the degree of damage inside the samples were uneven. At all the tested temperature, large damage is concentrated in the central area of the sample. From the cross-sectional view, the edge zone (marked in the figure) was severely damaged at temperature of 200 °C. As the temperature rose to 400 °C, significant damage occurred to the central zone of the sample. With further increase of temperature, the degree of damage tended to be uniform between the edge zone and the central zone. It showed slight damage at the top and bottom central zone, which contacted with top and bottom die. Through the thermo-mechanical FEM simulation, this study presents the stress and strain distribution inside the sample during compression deformation at elevated temperature, as well as the degree of damage to the sample revealing the high temperature mechanical behavior of Fe2Ni2CrAl1.3 MPEA.

4. Conclusion

In this work, the effect of Al content on the mechanical properties at elevated temperature of Fe2Ni2CrAlx (x = 0.9, 1.1, 1.2, 1.3 in molar ratio) MPEAs were investigated. The strength of the Fe2Ni2CrAlx MPEAs increased as the Al content increases. At high temperatures, the Fe2Ni2CrAl1.3 MPEA exhibits superior strength and good work hardening ability among the developed alloys, even up to 800 °C. Due to the low density, Fe2Ni2CrAl1.3 MPEA exhibits much higher specific yield strength values than most reported HEAs and conventional alloys. The fracture mechanism of Fe2Ni2CrAlx MPEAs is a combination of cleavage and slip separation. Recrystallized grains appeared during deformation at high temperature above 600 °C. FEM model results coupled with thermomechanical simulations provide the stress and strain field distribution within Fe2Ni2CrAl1.3 MPEA at different temperature. The degree of damage to the alloy under compressive load is evaluated, which can help to understand the high-temperature deformation behavior of Fe2Ni2CrAl1.3 MPEA. The lightweight Fe2Ni2CrAl1.3 MPEA demonstrates effective application in high-temperature fields.

CRediT authorship contribution statement

Ling Qiao: Writing – review & editing, Writing – original draft, Software, Methodology, Investigation, Formal analysis, Data curation. **Junya Inoue:** Writing – review & editing, Validation, Supervision. **R.V. Ramanujan:** Writing – review & editing, Supervision. **Kenji Sekido:** Methodology, Formal analysis. **Jingchuan Zhu:** Writing – review & editing, Supervision.

Declaration of competing interest

The authors declare that they have no known competing financial interests or personal relationships that could have appeared to influence the work reported in this paper.

Acknowledgments

This work is supported by JSPS Postdoctoral Fellowship for Research in Japan (No. P23045). It is also supported by AME Programmatic Fund by the Agency for Science, Technology and Research, Singapore under Grants No. A1898b0043 and A18B1b0061.

Data availability

The authors do not have permission to share data.

References

1. [1]

Li Weidong, Xie Di, Li Dongyue, Zhang Yong, Gao Yanfei, Liaw Peter K.
Mechanical behavior of high-entropy alloys
Prog. Mater. Sci., 118 (2021), Article 100777, 10.1016/j.pmatsci.2021.100777
View PDFView articleView in ScopusGoogle Scholar

2. [2]

Yeh J.W.
Alloy design strategies and future trends in high-entropy alloys
JOM, 35 (12) (2013), pp. 1759-1771, 10.1007/s11837-013-0761-6
View in ScopusGoogle Scholar

3. [3]

Yeh J.W., Chen S.K., Lin S.J., Gan J.Y., Chin T.S., Shun T.T., Tsau C.H., Chang S.Y.
Nanostructured high-entropy alloys with multiprincipal elements-novel alloy design concepts and outcomes
Adv. Eng. Mater., 6 (2004), pp. 299-303, 10.1002/adem.200300567
Google Scholar

4. [4]

Zhang W., Liaw P.K., Zhang Y.
Science and technology in high-entropy alloys
Sci. China Mater., 61 (1) (2018), pp. 2-22, 10.1007/s40843-017-9195-8
View in ScopusGoogle Scholar

5. [5]

Zhang Yong, Zuo Ting Ting, Tang Zhi, Gao Michael C., Dahmen Karin A., Liaw Peter K., Lu Zhao Ping
Microstructures and properties of high-entropy alloys
Prog. Mater. Sci., 61 (2014), pp. 1-93, 10.1016/j.pmatsci.2013.10.001
View PDFView articleGoogle Scholar

6. [6]

Zhang Mengdi, Zhang Lijun, Fan Jiantao, Yu Pengfei, Li Gong
Novel Co-free CrFeNiNb0.1Tix high-entropy alloys with ultra high hardness and strength
Mater. Sci. Eng. A, 764 (2019), Article 138212, 10.1016/j.msea.2019.138212
View PDFView articleView in ScopusGoogle Scholar

7. [7]

Wang Cheng, Li Tsung-Hsiung, Liao Yi-Chia, Li Chia-Lin, Jang Jason Shian-Ching, Hsueh Chun-Hway

Hardness and strength enhancements of CoCrFeMnNi high-entropy alloy with Nd doping
Mater. Sci. Eng. A, 764 (2019), Article 138192, 10.1016/j.msea.2019.138192
View PDFView articleView in ScopusGoogle Scholar
8. [8]
Tian Fuyang, Varga Lajos K., Chen Nanxian, Shen Jiang, Vitos Levente
Empirical design of single phase high-entropy alloys with high hardness
Intermetallics, 58 (2015), pp. 1-6, 10.1016/j.intermet.2014.10.010
View PDFView articleView in ScopusGoogle Scholar
9. [9]
Lv Shasha, Zu Yufei, Chen Guoqing, Zhao Bojun, Fu Xuesong, Zhou Wenlong
A multiple nonmetallic atoms co-doped CrMoNbWTi refractory high-entropy alloy with ultra-high strength and hardness
Mater. Sci. Eng. A, 795 (2020), Article 140035, 10.1016/j.msea.2020.140035
View PDFView articleView in ScopusGoogle Scholar
10. [10]
Průša Filip, Cabibbo Marcello, Šenková Alexandra, Kučera Vojtěch., Veselka Zbyněk., Školáková Andrea, Vojtěch Dalibor, Cibulková Jana, Čapek Jaroslav
High-strength ultrafine-grained CoCrFeNiNb high-entropy alloy prepared by mechanical alloying: Properties and strengthening mechanism
J. Alloys Compd., 835 (2020), Article 155308, 10.1016/j.jallcom.2020.155308
View PDFView articleView in ScopusGoogle Scholar
11. [11]
Ma L.L., Li X.W., Sun B.R., Xin S.W., Shen T.D.
Low activation V-Fe-Cr-Mn high-entropy alloys with exceptional strength
Mater. Sci. Eng. A, 860 (2022), Article 144243, 10.1016/j.msea.2022.144243
View PDFView articleView in ScopusGoogle Scholar
12. [12]
He Feng, Yang Zhongsheng, Liu Shaofei, Chen Da, Lin Weitong, Yang Tao, Wei Daixiu, Wang Zhijun, Wang Jincheng, Kai Ji-jung.
Strain partitioning enables excellent tensile ductility in precipitated heterogeneous high-entropy alloys with gigapascal yield strength
Int. J. Plast., 144 (2021), Article 103022, 10.1016/j.ijplas.2021.103022
View PDFView articleView in ScopusGoogle Scholar
13. [13]
Liu Dong, *et al.*
Exceptional fracture toughness of CrCoNi-based medium- and high-entropy alloys at 20 kelvin
Science, 378 (2022), pp. 978-983, 10.1126/science.abp8070
View in ScopusGoogle Scholar
14. [14]
Wei Qi, Zhang Aijun, Han Jiesheng, Xin Benbin, Su Bo, Wang Xiaochao, Meng Junhu
A novel Hf30Nb25Ta25Ti15Mo5 refractory high entropy alloy with excellent combination of strength and ductility
Mater. Sci. Eng. A, 857 (2022), Article 144035, 10.1016/j.msea.2022.144035
View PDFView articleView in ScopusGoogle Scholar

15. [15]
Lin Danyang, Xi Xin, Li Xiaojie, Hu Jixu, Xu Lianyong, Han Yongdian, Zhang Yankun, Zhao Lei
High-temperature mechanical properties of FeCoCrNi high-entropy alloys fabricated via selective laser melting
Mater. Sci. Eng. A, 832 (2022), Article 142354, 10.1016/j.msea.2021.142354
View PDFView articleView in ScopusGoogle Scholar
16. [16]
Cao B.X., Yang T., Fan L., Luan J.H., Jiao Z.B., Liu C.T.
Refractory alloying additions on the thermal stability and mechanical properties of high-entropy alloys
Mater. Sci. Eng. A, 797 (2020), Article 140020, 10.1016/j.msea.2020.140020
View PDFView articleView in ScopusGoogle Scholar
17. [17]
Zheng Weijie, Shulin L., Wu Shusen, Chen Xiaohua, Guo Wei
Development of MoNbVTax refractory high entropy alloy with high strength at elevated temperature
Mater. Sci. Eng. A, 850 (2022), Article 143554, 10.1016/j.msea.2022.143554
View PDFView articleView in ScopusGoogle Scholar
18. [18]
Kim Y.K., Yang S., Lee K.A.
Superior temperature-dependent mechanical properties and deformation behavior of equiatomic CoCrFeMnNi high-entropy alloy additively manufactured by selective laser melting
Sci. Rep., 10 (2020), p. 8045, 10.1038/s41598-020-65073-2
View in ScopusGoogle Scholar
19. [19]
Nabizada A., Zarei-Hanzaki A., Abedi H.R., Barati M.H., Asghari-Rad P., Kim H.S.
The high temperature mechanical properties and the correlated microstructure/texture evolutions of a TWIP high entropy alloy
Mater. Sci. Eng. A, 802 (2021), Article 140600, 10.1016/j.msea.2020.140600
View PDFView articleView in ScopusGoogle Scholar
20. [20]
Liu X.W., Gao N., Zheng J., Wu Y., Zhao Y.Y., Chen Q., Zhou W., Pu S.Z., Jiang W.M., Fan Z.T.
Improving high-temperature mechanical properties of cast CrFeCoNi high-entropy alloy by highly thermostable in-situ precipitated carbides
J. Mater. Sci. Technol., 72 (2021), pp. 29-38, 10.1016/j.jmst.2020.07.016
View PDFView articleView in ScopusGoogle Scholar
21. [21]
Wei Wenchao, Wang Tao, Wang Chunyu, Wu Meng, Nie Yunpeng, Peng Jun, Ductile W.
0.4MoNbxTaTi refractory high-entropy alloys with excellent elevated temperature strength
Mater. Lett., 295 (2021), Article 129753, 10.1016/j.matlet.2021.129753
View PDFView articleView in ScopusGoogle Scholar
22. [22]
Vaidya M., Anupam Ameey, Vijay Bharadwaj J., Srivastava Chandan, Murty B.S.
Grain growth kinetics in CoCrFeNi and CoCrFeMnNi high entropy alloys processed by spark plasma sintering
J. Alloys Compd., 791 (2019), pp. 1114-1121, 10.1016/j.jallcom.2019.03.341

View PDFView articleView in ScopusGoogle Scholar
23. [23]
Nazaretyan Kh., Aydinyan S., Kirakosyan H., Moskovskikh D., Nepapushev A., Kuskov K., Tumanyan M., Zargaryan A., Traksmaa R., Kharatyan S.
AlCo-rich AlCoNiFe and AlCoNiFeCr high entropy alloys: Synthesis and interaction pathway at high heating rates
J. Alloys Compd., 931 (2023), Article 167589, 10.1016/j.jallcom.2022.167589
View PDFView articleView in ScopusGoogle Scholar
24. [24]
Yang Xuehui, Zhang Jian, Sagar Sugrim, Dube Tejesh, Kim Bong-Gu, Jung Yeon-Gil, Koo Dan Daehyun, Jones Alan, Zhang Jing
Molecular dynamics modeling of mechanical and tribological properties of additively manufactured AlCoCrFe high entropy alloy coating on aluminum substrate
Mater. Chem. Phys., 263 (2021), Article 124341, 10.1016/j.matchemphys.2021.124341
View PDFView articleView in ScopusGoogle Scholar
25. [25]
Meghwal Ashok, Anupam Ameey, Luzin Vladimir, Schulz Christiane, Hall Colin, Murty B.S., Kottada R avi Sankar, Berndt Christopher C., Ang Andrew Siao Ming
Multiscale mechanical performance and corrosion behaviour of plasma sprayed AlCoCrFeNi high-entropy alloy coatings
J. Alloys Compd., 854 (2021), Article 157140, 10.1016/j.jallcom.2020.157140
View PDFView articleView in ScopusGoogle Scholar
26. [26]
Sim R.K., Xu Z., Wu M.Y., *et al.*
Microstructure, mechanical properties, corrosion and wear behavior of high-entropy alloy AlCoCrFeNix (x>0 the) and medium-entropy alloy (x=0)
J. Mater. Sci., 57 (2022), pp. 11949-11968, 10.1007/s10853-022-07256-y
View in ScopusGoogle Scholar
27. [27]
Zhang G.J., Tian Q.W., Yin K.X., Niu S.Q., Wu M.H., Wang W.W., Wang Y.N., Huang J.C.
Effect of Fe on microstructure and properties of AlCoCrFexNi (x=1.5, 2.5) high entropy alloy coatings prepared by laser cladding
Intermetallics, 119 (2020), Article 106722, 10.1016/j.intermet.2020.106722
View PDFView articleView in ScopusGoogle Scholar
28. [28]
Ostrowska Marlena, Riani Paola, Bocklund Brandon, Liu Zi-Kui, Cacciamani Gabriele
Thermodynamic modeling of the Al-Co-Cr-Fe-Ni high entropy alloys supported by key experiments
J. Alloys Compd., 897 (2022), Article 162722, 10.1016/j.jallcom.2021.162722
View PDFView articleView in ScopusGoogle Scholar
29. [29]
Hou Jinxiong, Shi Xiaohui, Qiao Junwei, Zhang Yong, Liaw Peter K., Wu Yucheng
Ultrafine-grained dual phase Al0.45CoCrFeNi high-entropy alloys
Mater. Des., 180 (2019), Article 107910, 10.1016/j.matdes.2019.107910
View PDFView articleView in ScopusGoogle Scholar

30. [30]
Estrada-Guel I., Rodríguez-Gonz lez C.A., Hernández-Paz J., Jimenez O., Santos-Beltran A., Mart nez Sánchez R., Romero-Romero M., Gómez-Esparza C.D.
Phase composition and its effect on the mechanical performance of an AlCoCrFeNiTi high-entropy alloy
Mater. Lett., 316 (2022), Article 132035, 10.1016/j.matlet.2022.132035
View PDFView articleView in ScopusGoogle Scholar
31. [31]
Jiao Z.M., Ma S.G., Chu M.Y., *et al.*
Superior mechanical properties of AlCoCrFeNiTi x high-entropy alloys upon dynamic loading
J. Mater. Eng. Perform., 25 (2016), pp. 451-456, 10.1007/s11665-015-1869-3
View in ScopusGoogle Scholar
32. [32]
Qi Wu, Wang Wenrui, Yang Xiao, Zhang Guannan, Ye Wei, Su Yitian, Li Yong, Chen Shuying
Effects of Al and Ti co-doping on the strength-ductility-corrosion resistance of CoCrFeNi-AlTi high-entropy alloys
J. Alloys Compd., 925 (2022), Article 166751, 10.1016/j.jallcom.2022.166751
View PDFView articleView in ScopusGoogle Scholar
33. [33]
Wang Woei-Ren, Wang Wei-Lin, Yeh Jien-Wei
Phases, microstructure and mechanical properties of AlxCoCrFeNi high-entropy alloys at elevated temperatures
J. Alloys Compd., 589 (2014), pp. 143-152, 10.1016/j.jallcom.2013.11.084
View PDFView articleView in ScopusGoogle Scholar
34. [34]
Ge Shaofan, Fu Huameng, Zhang Long, Mao Huahai, Li Hong, Wang Aimin, Li Weirong, Zhang Haifen g
Effects of Al addition on the microstructures and properties of MoNbTaTiV refractory high entropy alloy
Mater. Sci. Eng. A, 784 (2020), Article 139275, 10.1016/j.msea.2020.139275
View PDFView articleView in ScopusGoogle Scholar
35. [35]
Kim W.J., Jeong H.T., Park H.K., Park K., Na T.W., Choi E.
The effect of Al to high-temperature deformation mechanisms and processing maps of Al0.5CoCrFeMnNi high entropy alloy
J. Alloys Compd., 802 (2019), pp. 152-165, 10.1016/j.jallcom.2019.06.099
View PDFView articleView in ScopusGoogle Scholar
36. [36]
Shi Yunzhu, Yang Bin, Rack Philip D., Guo Shifeng, Liaw Peter K., Zhao Ying
High-throughput synthesis and corrosion behavior of sputter-deposited nanocrystalline Alx(CoCrFeNi)100-x combinatorial high-entropy alloys
Mater. Des., 195 (2020), Article 109018, 10.1016/j.matdes.2020.109018
View PDFView articleView in ScopusGoogle Scholar
37. [37]
Li Meiyan, Zhang Qi, Han Bin, Song Lixin, Li Jianlong, Yang Jie

Investigation on microstructure and properties of AlxCoCrFeMnNi high entropy alloys by ultrasonic impact treatment
J. Alloys Compd., 816 (2020), Article 152626, 10.1016/j.jallcom.2019.152626
View PDFView articleView in ScopusGoogle Scholar
38. [38]
Rahul M.R., Samal Sumanta, Venugopal S., Phanikumar Gandham
Experimental and finite element simulation studies on hot deformation behaviour of AlCoCrFeNi2.1 eutectic high entropy alloy
J. Alloys Compd., 749 (2018), pp. 1115-1127, 10.1016/j.jallcom.2018.03.262
View PDFView articleView in ScopusGoogle Scholar
39. [39]
Qiao Ling, Ramanujan R.V., Zhu Jingchuan
Discovery of new Fe2Ni2CrAlx multi-principal element alloys with promising mechanical properties
J. Mater. Res. Technol., 24 (2023), pp. 3996-4008, 10.1016/j.jmrt.2023.04.015
View PDFView articleView in ScopusGoogle Scholar
40. [40]
Li G.R., Wei Y.M., Wang H.M., Zhou Z.C., Su W.X., Dong C., Zhang Z.B.
Microstructure and properties of FeCoNi1.5CrCup/Al high-entropy alloy strengthened aluminum matrix composites and finite element simulation
Mater. Today Commun., 35 (2023), Article 106022, 10.1016/j.mtcomm.2023.106022
View PDFView articleView in ScopusGoogle Scholar
41. [41]
Li Hongge, Huang Yongjiang, Jiang Songshan, Lu Yunzhuo, Gao Xiaoyu, Lu Xing, Ning Zhiliang, Sun Jianfei
Columnar to equiaxed transition in additively manufactured CoCrFeMnNi high entropy alloy
Mater. Des., 197 (2021), Article 109262, 10.1016/j.matdes.2020.109262
View PDFView articleView in ScopusGoogle Scholar
42. [42]
Ahn Soung Yeoul, Kim Dong Geun, Lee Jeong Ah, Kim Eun Seong, Jeong Sang Guk, Kim Rae Eon, Choe Jungho, Hong Soon-Jik, Quang Pham, Lee Sunghak, Kim Hyoung Seop
Dynamic compression behavior of CoCrFeMnNi high-entropy alloy fabricated by direct energy deposition additive manufacturing
J. Alloys Compd., 960 (2023), Article 170602, 10.1016/j.jallcom.2023.170602
View PDFView articleView in ScopusGoogle Scholar
43. [43]
Qiao Ling, Ramanujan R.V., Zhu Jingchuan
Machine learning discovery of a new cobalt free multi-principal-element alloy with excellent mechanical properties
Mater. Sci. Eng. A, 845 (2022), Article 143198, 10.1016/j.msea.2022.143198
View PDFView articleView in ScopusGoogle Scholar
44. [44]
Roy Shibayan, Suwas Satyam
The influence of temperature and strain rate on the deformation response and microstructural evolution during hot compression of a titanium alloy Ti-6Al-4V-0.1B

J. Alloys Compd., 548 (2013), pp. 110-125, 10.1016/j.jallcom.2012.08.123
View PDFView articleView in ScopusGoogle Scholar

45. [45]

Lei Liming, Huang Xu, Wang Minmin, Wang Liqiang, Qin Jining, Li Hongping, Lu ShiQiang
Effect of hot compressive deformation on the martensite transformation of Ti-10V-2Fe-3Al titanium alloy
Mater. Sci. Eng. A, 530 (2011), pp. 591-601, 10.1016/j.msea.2011.10.028
View PDFView articleView in ScopusGoogle Scholar

46. [46]

Shah Naishalkumar, Rahul M.R., Bysakh Sandip, Phanikumar Gandham
Microstructure stability during high temperature deformation of CoCrFeNiTa eutectic high entropy alloy through nano-scale precipitation
Mater. Sci. Eng. A, 824 (2021), Article 141793, 10.1016/j.msea.2021.141793
View PDFView articleView in ScopusGoogle Scholar

47. [47]

Zhao Shuangqun, Xie Xishan, Smith Gaylord D., Patel Shailesh J.
Microstructural stability and mechanical properties of a new nickel-based superalloy
Mater. Sci. Eng. A, 355 (1–2) (2003), pp. 96-105, 10.1016/S0921-5093(03)00051-0
View PDFView articleView in ScopusGoogle Scholar

48. [48]

Sakai Taku, Belyakov Andrey, Kaibyshev Rustam, Miura Hiromi, Jonas John J.
Dynamic and post-dynamic recrystallization under hot, cold and severe plastic deformation conditions
Prog. Mater. Sci., 60 (2014), pp. 130-207, 10.1016/j.pmatsci.2013.09.002
View PDFView articleView in ScopusGoogle Scholar

49. [49]

Stepanov N.D., Shaysultanov D.G., Yurchenko N.Yu., Zherebtsov S.V., Ladygin A.N., Salishchev G.A., Tikhonovsky M.A.
High temperature deformation behavior and dynamic recrystallization in CoCrFeNiMn high entropy alloy
Mater. Sci. Eng. A, 636 (2015), pp. 188-195, 10.1016/j.msea.2015.03.097
View PDFView articleView in ScopusGoogle Scholar

50. [50]

Alijani F., Reihanian M., Gheisari Kh., Miyamoto H.
Microstructure and high-temperature deformation behavior of FeCoNiMnV high entropy alloy
Mater. Chem. Phys., 256 (2020), Article 123675, 10.1016/j.matchemphys.2020.123675
View PDFView articleView in ScopusGoogle Scholar

51. [51]

Philippart I., Rack H.J.
High temperature dynamic yielding in metastable Ti-6.8Mo-4.5F-1.5Al
Mater. Sci. Eng. A, 243 (1998), pp. 196-200, 10.1016/S0921-5093(97)00800-9
View PDFView articleView in ScopusGoogle Scholar

52. [52]

Lin Y.C., Wu X.-Y., Chen X.-M., Chen J., Wen D.-X., Zhang J.-L., Li L.-T.

EBSD study of a hot deformed nickel-based superalloy
J. Alloys Compd., 640 (2015), pp. 101-113, 10.1016/j.jallcom.2015.04.008
View PDFView articleView in ScopusGoogle Scholar

53. [53]
Dudova N., Belyakov A., Sakai T., Kaibyshev R.
Dynamic recrystallization mechanisms operating in a Ni-20%Cr alloy under hot-to-warm working
Acta Mater., 58 (10) (2010), pp. 3624-3632, 10.1016/j.actamat.2010.02.032
View PDFView articleView in ScopusGoogle Scholar

54. [54]
Wang Xin, Zhang Yunpeng, Ma Xuelong
High temperature deformation and dynamic recrystallization behavior of AlCrCuFeNi high entropy alloy
Mater. Sci. Eng. A, 778 (2020), Article 139077, 10.1016/j.msea.2020.139077
View PDFView articleView in ScopusGoogle Scholar

55. [55]
Zhao C., Chen X., Pan F., Gao S., Zhao D., Liu X.
Effect of sn content on strain hardening behavior of as-extruded Mg-Sn alloys
Mater. Sci. Eng. A, 713 (2018), pp. 244-252, 10.1016/j.msea.2017.12.074
View PDFView articleView in ScopusGoogle Scholar

56. [56]
Yang M.X., Yuan F.P., Xie Q.G., Wang Y.D., Ma E., Wu X.L.
Strain hardening in Fe-16Mn-10Al-0.86C-5Ni high specific strength steel
Acta Mater., 109 (2016), pp. 213-222, 10.1016/j.actamat.2016.02.044
View PDFView articleView in ScopusGoogle Scholar